Simulating Postfire Debris Flow Runout Using Morphodynamic Models and Stochastic Surrogates

Elaine T. Spiller[1], Luke A. McGuire[2], Palak Patel[3], Abani Patra[3], E. Bruce Pitman[4]

[1]Department of Mathematical and Statistical Sciences, Marquette University, Milwaukee, Wisconsin, USA
[2]Department of Geosciences, University of Arizona, Tucson, Arizona, USA
[3]Data Intensive Studies Center, Tufts University, Medford, Massachusetts, USA
[4]Department of Materials Design and Innovation, University at Buffalo, Buffalo, New York, USA

Key Points:

- We simulate postfire debris-flow runout by accelerating and building surrogates for a morphodynamic model of runoff and sediment transport.
- With this acceleration, we can rapidly explore how postfire recovery influences debris flow runout as a function of time since fire.
- Surrogate-based postfire hazard analyses offer rapid assessments of downstream debris flow inundation due to forecast or design rainstorms.

Corresponding author: Elaine T. Spiller, `elaine.spiller@marquette.edu`

Abstract

Fire affects soil and vegetation, which in turn can promote the initiation and growth of runoff-generated debris flows in steep watersheds. Postfire hazard assessments often focus on identifying the most likely watersheds to produce debris flows, quantifying rainfall intensity-duration thresholds for debris flow initiation, and estimating the volume of potential debris flows. This work seeks to expand on such analyses and forecast downstream debris flow runout and peak flow depth. Here, we report on a high fidelity computational framework that enables debris flow simulation over two watersheds and the downstream alluvial fan, although at significant computational cost. We also develop a Gaussian Process surrogate model, allowing for rapid prediction of simulator outputs for untested scenarios. We utilize this framework to explore model sensitivity to rainfall intensity and sediment availability as well as parameters associated with saturated hydraulic conductivity, hydraulic roughness, grain size, and sediment entrainment. Simulation results are most sensitive to peak rainfall intensity and hydraulic roughness. We further use this approach to examine variations in debris flow inundation patterns at different stages of postfire recovery. Sensitivity analysis indicates that constraints on temporal changes in hydraulic roughness, saturated hydraulic conductivity, and grain size following fire would be particularly beneficial for forecasting debris flow runout throughout the postfire recovery period. The emulator methodology presented here also provides a means to compute the probability of a debris flow inundating a specific downstream region, consequent to a forecast or design rainstorm. This workflow could be employed in scenario-based planning for postfire hazard mitigation.

Plain Language Summary

Fire on steep hillslopes increases the potential for debris flows, or rapidly moving mixtures of water, soil, ash, and rock, that can develop during intense rainfall. Debris flows threaten communities situated downstream of steep, burned areas. Burn severity and hillslope steepness give some indication of the potential for debris flow initiation in response to a particular rainstorm, but these factors alone do not indicate which downstream areas might be inundated by a flow. To investigate areas impacted by potential debris flows, we utilize a computational model that represents the physical processes of debris flow initiation and runout. Such process-based models are computationally intensive, which has limited their use in rapid hazard assessments. Here, we implement a de-

bris flow initiation and runout model in a high-performance computing framework. Even so, a typical debris flow simulation takes several hours to complete on a supercomputer. Thus, we also build statistical models of these physical models, so-called emulators. Emulators can rapidly approximate the debris flow simulation and thus offer a mechanism to investigate outcomes of debris flow models over a wide range of scenarios. We investigate how debris flow inundation footprints vary with rainfall intensity and the impact of landscape recovery on debris flows.

1 Introduction

Fire alters soil and vegetation, leading to increases in runoff and erosion (Shakesby & Doerr, 2006; Moody et al., 2013). In extreme cases, particularly when steep watersheds burn at moderate or high severity, rapid entrainment of sediment into runoff can produce debris flows (Kean et al., 2011; Gabet & Bookter, 2008; Esposito et al., 2023; Conedera et al., 2003; Nyman et al., 2011; Diakakis et al., 2023). Postfire debris flows generated by runoff are most common in the first year following fire, when fire-driven reductions in soil infiltration capacity, rainfall interception, and hydraulic roughness are most extreme (DeGraff et al., 2015; Hoch et al., 2021; Thomas et al., 2021; Esposito et al., 2023; Graber et al., 2023). Due to the complex interactions among runoff, sediment transport, and debris-flow initiation and runout following fire, mathematical models that couple these processes have the potential to inform our understanding of postfire debris-flow hazards and how they change through time as landscapes recover (McGuire et al., 2021). Yet the exploration of postfire debris flow processes through application of morphodynamic models for runoff and sediment transport is often limited by the high dimensionality, poor constraints on parameters, and substantial computation time of the models. Quantification of uncertainties associated with sources and model parameters, and incorporation of those uncertainties in probabilistic predictions of hazard, often require use of simulation ensembles with hundreds or thousands of members, greatly increasing computational costs (Bayarri et al., 2015). In this work, we accelerate a recently developed morphodynamic model of runoff and sediment transport (McGuire et al., 2017), and pair model runs with stochastic surrogates for high-dimensional output (Gu & Berger, 2016) as a strategy for simulating postfire debris-flow runout. This acceleration also enables us to rapidly explore how temporal changes in fire-affected model input parameters influence debris flow runout.

The processes leading to the initiation and growth of runoff-generated debris flows following fire involve the generation of spatially distributed overland flow and its subsequent interaction with sediment on hillslopes and in channels (Santi et al., 2008; Staley et al., 2014; McGuire et al., 2017; Guilinger et al., 2020). This presents a contrast to debris flows that mobilize from shallow landslides, which initiate when infiltration promotes increases in pore-water pressure that causes a discrete mass of soil to become unstable on a hillslope (Iverson et al., 1997). The source of sediment for postfire runoff-generated debris flows may come from a combination of processes, including widespread, shallow erosion on hillslopes in response to raindrop-driven sediment transport and unconfined sheet flow, rill erosion on hillslopes in areas of concentrated flow, and channel scour (Santi et al., 2008; Staley et al., 2014; McGuire et al., 2017; Tang et al., 2019). All three processes are more efficient at eroding sediment following fire as a result of decreases in ground cover and increases in runoff (Robichaud et al., 2016), particularly rill and channel erosion processes where overland flow does the work to entrain and transport sediment (Sheridan et al., 2007; Wagenbrenner et al., 2010). In areas of unconfined, shallow flow, raindrops facilitate sediment detachment and transport in combination with runoff (Kinnell, 2005). Raindrop-driven sediment transport on hillslopes increases following fire due to removal of the vegetation canopy, litter, and duff, that tend to shield the soil surface from raindrop impact in unburned settings.

Models designed to simulate runoff-generated debris flows from initiation to deposition must therefore account for spatially distributed runoff and sediment transport as well as changes in flow behavior resulting from spatial and temporal variations in sediment concentration. Fully developed debris flows are characterized by volumetric sediment concentrations in excess of 40-50%, though they initiate from runoff with initially negligible sediment concentration. Due, in part, to the relatively flashy hydrologic response of watersheds burned by fire, postfire runoff-generated debris flows initiate in response to short-duration bursts of high intensity rainfall (Kean et al., 2011). Rainfall intensity averaged over a 15-minute time period, I_{15}, is correlated well with runoff magnitude at the outlet of small, recently burned watersheds and threshold values of I_{15} have proven to be reasonable predictors for debris flow initiation in the western USA (Kean et al., 2011; Staley et al., 2017). Rainstorms that contain multiple, distinct bursts of high intensity rainfall, such as where I_{15} exceeds the debris flow threshold at multiple times in a single event, may lead to multiple pulses of debris flow activity (Kean et al., 2011).

One benefit of morphodynamic models that are capable of simulating the debris-flow lifecycle from initiation to runout is their ability to directly account for the impacts of temporally varying rainfall intensity on debris flow processes, including runout and inundation extent. In contrast, models designed only to simulate debris flow runout processes (i.e. neglecting runoff and sediment transport), can be employed by defining an inflow hydrograph above the anticipated runout zone based on the rainfall hydrograph and an estimated debris flow volume, or by allowing a pile of sediment and water to flow downstream from a pre-defined initiation zone (Barnhart et al., 2021; Gorr et al., 2022; Gibson et al., 2022). As a result, employing morphodynamics models to estimate debris flow runout avoids introducing epistemic uncertainty associated with specifying a volume of material associated with an inflow hydrograph.

McGuire et al. (2017) developed a model that accounts for infiltration, runoff, sediment transport, and changes to flow resistance driven by sediment concentration in order to simulate postfire debris flow initiation and growth. In this model, rainfall drives sediment entrainment and transport processes that naturally lead to debris flow initiation when hydrogeomorphic conditions give rise to flows with sufficiently high sediment concentrations. Since rainfall, runoff, and erosion processes are related to model parameters known to change following fire, such as saturated hydraulic conductivity (Perkins et al., 2022; Ebel et al., 2022; Thomas et al., 2021), hydraulic roughness (Stoof et al., 2015), and vegetation cover (Stoof et al., 2012), it is possible to use this framework to explore how postfire recovery affects debris-flow initiation, growth, and runout. The model proposed by McGuire et al. (2017) contains a number of parameters that are challenging to constrain and is computationally intensive, especially when simulating debris flow initiation and runout processes over large areas. Thus far, model applications have been limited to examining debris-flow initiation processes in small headwater basins where prior work and intensive field monitoring helped constrain parameter values (McGuire et al., 2021, 2017; Tang et al., 2019). Here, we employ adaptive mesh refinement and parallel computations from the Titan framework (Patra et al., 2005; Dalbey et al., 2008) to make model application more tractable over larger spatial domains, specifically with the goal of simulating the entirety of the postfire debris-flow lifecycle from runoff generation and debris flow growth to runout. In addition, we employ statistical emulators, which enable fast approximations to solutions of the model equations, in order to explore the influence of model parameters on debris-flow runout extent.

Gaussian process emulators (GPs) are a powerful class of statistical surrogates that enable rapid approximation and uncertainty quantification of computationally intensive first principles (conservation laws) based models or, *simulators* (Currin et al., 1988; Sacks, Welch, et al., 1989; Welch et al., 1992). In the context of postfire debris-flows, GPs offer a mechanism to quickly explore spatial patterns in peak flow depth and area inundated for various parameter settings. GPs also allow for uncertainty quantification via Monte Carlo (MC) simulations of flow inundation. Along the way, GPs offer an approximate sensitivity analysis of physical parameters' effects on debris-flow inundation. Parallel partial emulation (PPE) (Gu & Berger, 2016) extends the GP methodology to vector-valued outputs – in our case, flow depth at each map point (pixel). Some recent studies use PPE for flow model sensitivity analysis and calibration (Zhao et al., 2021; Zhao & Kowalski, 2022). In this work, we apply PPE to explore the effects of rainfall intensity and sediment availability as well as parameters associated with saturated hydraulic conductivity, hydraulic roughness, grain size, and sediment entrainment on peak debris flow depth and inundation extent.

2 Study Area

The Thomas Fire ignited in December 2017 and burned more than 1100 km^2, including a series of steep watersheds in the Santa Ynez Mountains above the community of Montecito, USA (Figure 1a). On 9 January 2018, widespread rainfall developed over the burned area in association with an atmospheric river (Oakley et al., 2018). A narrow cold frontal rainband (NCFR), a relatively small-scale feature characterized by a band of intense precipitation that forms along a cold front, moved over burned watersheds above Montecito and produced a short-duration burst of intense rainfall. Peak 15-minute rainfall intensities, I_{15}, in this area ranged from approximately 78 mm/h to 105 mm/h (Kean et al., 2019). During this time period, rainfall intensities greatly exceeded the infiltration capacity of the soil, leading to infiltration-excess overland flow that generated rills on steep hillslopes (Alessio et al., 2021). The combination of intense hillslope erosion and channel incision led to runoff-generated debris flows that traveled across the populated alluvial fan (Kean et al., 2019; Morell et al., 2021; Alessio et al., 2021). The debris flows that initiated in six watersheds above Montecito mobilized more than 630,000 m^3 of sediment and led to 23 fatalities, 408 damaged structures, and more than $1 billion in damage (Kean et al., 2019; Lancaster et al., 2021). In this study, we focus on modeling de-

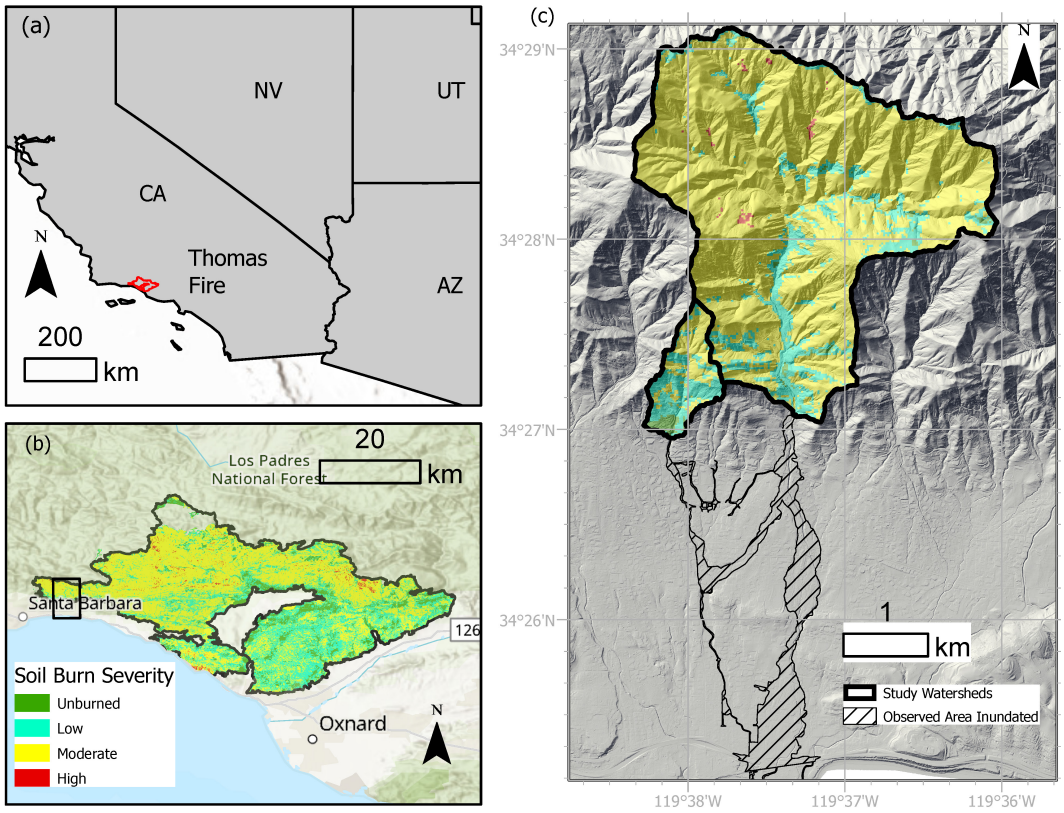

Figure 1. (a) The Thomas Fire ignited on 4 December 2017 and burned over 1140 km^2 in southern California, USA. (b) The western portion of the burned area included a series of steep watersheds (black rectangle) above the community of Montecito, located near Santa Barbara. (c) Our study focuses on two watersheds, Oak Creek (0.45 km^2) and San Ysidro Creek (7.6 km^2), located upstream of Montecito.

bris flow initiation, growth, and runout for two of these watersheds, Oak Creek and San Ysidro Creek. These watersheds are well suited for our study since high resolution topographic and rainfall data are available and we can leverage data collection following the fire (Kean et al., 2019) and previous work in the Transverse Ranges of southern California (McGuire et al., 2016, 2021; Tang et al., 2019; McGuire et al., 2017) to constrain model parameter ranges. In addition, the model domain, which includes the watersheds and downstream alluvial fan, is large enough to make physics-based simulations computationally challenging (Figure 1c).

Roughly 85% of San Ysidro Creek, which has a total drainage area of 7.6 km^2, burned at moderate or high severity (Figure 1c). Approximately 49% of Oak Creek, which is sub-

stantially smaller at 0.45 km^2, burned at moderate or high severity. Both the San Ysidro and Oak Creek watersheds are steep, with median slopes of 28 and 21 degrees, respectively. The debris flow that initiated in San Ysidro Creek mobilized a total volume of 297,000 m^3 and inundated an area of 905,000 m^2 while the smaller Oak Creek watershed produced a debris flow that moved $10,000$ m^3 of sediment and inundated $102,000$ m^2 (Kean et al., 2019) (Figure 1c). The grain size distribution in the debris flows was bimodal, consisting of a sandy matrix that suspended boulders with a large axis greater than several meters (Kean et al., 2019).

3 Methodology

3.1 Simulating runoff-generated debris flows with Titan2D

Steep watersheds recently burned by fire often experience greater amounts of runoff and increased rates of sediment transport. Factors affecting rates of sediment transport, and also the initiation and growth of runoff-generated debris flows, include rainfall intensity and duration, vegetation cover, soil infiltration capacity, and sediment characteristics (e.g. grain size, erodibility). The model developed by McGuire et al. (2017) represents rainfall, infiltration, fluid flow, and sediment entrainment and deposition processes, which makes it a useful framework for simulating runoff-generated debris flows in steep terrain (McGuire et al., 2017; Tang et al., 2020). We provide a brief overview of the governing equations, which we solve within the Titan2D framework (Patra et al., 2005; Simakov et al., 2019).

The Titan2D code employs an adaptive mesh, finite volume scheme to solve hyperbolic PDEs describing shallow-water like mass flows over digital elevation models of real topography. Titan2D (Patra et al., 2005) was originally developed to solve the depth averaged shallow-water mass flow equations by Savage and Hutter (1989). Titan was modernized and restructured in 2019 (Simakov et al., 2019) to optimize storage and access for parallel adaptive mesh refinement, and to facilitate the usage of new material models. Using Titan2D to solve the model equations proposed by McGuire et al. (2017) therefore offers several advantages, especially for simulating debris flows over spatial scales of more than a few square kilometers. In particular, Titan2D uses *partitioned hash-tables* for better memory allocation structures, allowing it to compute over a large domain employing adaptive mesh refinement (AMR) and unrefinement, with computational efficiency.

219 It is also well suited for parallel computing using MPI and OpenMP and dynamic load
220 balancing for exploiting multiprocessor computing. The computational efficiencies at-
221 tained make it tractable to simulate end-to-end flows from initiation to downstream in-
222 undation.

223 The equations representing the motion of fluid and sediment can be written as a
224 set of depth averaged conservation laws. We have

225 $$\frac{\partial \mathbf{U}}{\partial t} + \frac{\partial \mathbf{F}}{\partial x} + \frac{\partial \mathbf{G}}{\partial y} = \mathbf{S_0} + \mathbf{S_1} + \mathbf{S_2}, \tag{1}$$

226 where

227 $$\mathbf{U} = \left\{ h \quad uh \quad vh \quad c_1 h \quad \cdots \quad c_k h \right\}^T, \tag{2}$$

228 $$\mathbf{F} = \left\{ hu \quad hu^2 + \tfrac{1}{2} g_z h^2 \quad huv \quad huc_1 \quad \cdots \quad huc_k \right\}^T, \tag{3}$$

229 $$\mathbf{G} = \left\{ hv \quad huv \quad hv^2 + \tfrac{1}{2} g_z h^2 \quad hvc_1 \quad \cdots \quad hvc_k \right\}^T, \tag{4}$$

230 and where h, u, v, and c_i are flow depth, velocity along x-axis, velocity along y- axis,
231 and sediment concentration of particle size class i. Components of gravitational accel-
232 eration in the x, y, and z directions are given by g_x, g_y, and g_z, respectively, and k de-
233 notes the number of particle size classes. $\mathbf{S_0}$, $\mathbf{S_1}$ and $\mathbf{S_2}$ are source terms. $\mathbf{S_0}$ denotes
234 the contributions of mass sources and sinks associated with the effective rainfall rate, P_{eff},
235 and the soil infiltration capacity, I, as well as momentum sources and sinks arising from
236 variations in topographic elevation, and spatial variations in sediment concentration and
237 debris flow resistance terms, S_x and S_y. Specifically, $\mathbf{S_0}$ is given as

238 $$\mathbf{S_0} = \begin{Bmatrix} P_{eff} - I + \frac{\partial z}{\partial t} \\ -g_x h + \gamma_x - \psi S_x \\ -g_y h + \gamma_y - \psi S_y \\ 0 \\ \vdots \\ 0 \end{Bmatrix}. \tag{5}$$

The debris flow resistance terms are scaled by ψ, which increases linearly from 0 to 1 as the volumetric sediment concentration increases from 0.2 to 0.4. This scaling factor gradually increases the importance of the debris flow resistance terms as volumetric sediment concentration approaches levels that are consistent with a transition from with flood flow to debris flow. The terms γ_x and γ_y account for the effects of spatially variable sediment

concentration and are given by

$$\gamma_x = \frac{-(\rho_s - \rho_w) g_z h^2}{2\rho_f} \frac{\partial c}{\partial x} \tag{6}$$

and

$$\gamma_y = \frac{-(\rho_s - \rho_w) g_z h^2}{2\rho_f} \frac{\partial c}{\partial y} \tag{7}$$

Here, c denotes volumetric sediment concentration, $\rho_w = 1000$ kg m^{-3} the density of water, $\rho_s = 2600$ kg m^{-3} the density of sediment, and $\rho_f = c\rho_f + (1-c)\rho_w$ the density of the flow. $\mathbf{S_1}$ accounts for flow resistance using a depth-dependent Manning's formulation, and is given as

$$\mathbf{S_1} = \begin{Bmatrix} 0 \\ g_z \eta^2 h u \sqrt{hu^2 + hv^2}/h^{7/3} \\ g_z \eta^2 h v \sqrt{hu^2 + hv^2}/h^{7/3} \\ 0 \\ \vdots \\ 0 \end{Bmatrix}, \tag{8}$$

where η is the Manning friction coefficient. The friction coefficient varies with flow depth according to

$$\eta = \begin{cases} \eta_0 \left(h/h_c\right)^{-\epsilon} & h \leq h_c \\ \eta_0 & h > h_c \end{cases}, \tag{9}$$

where η_0 is the hydraulic roughness coefficient, h_c is a critical flow depth and ϵ is a phenomenological exponent. Soil infiltration capacity, I, is represented by the Green-Ampt model where

$$I = k_s \frac{Z_f + h_f + h}{Z_f}, \tag{10}$$

with k_s denoting saturated hydraulic conductivity, h_f the wetting front potential, $Z_f = V/(\theta_s - \theta_i)$ the depth of the wetting front, V the cumulative infiltrated depth, θ_s the volumetric soil moisture content at saturation, and θ_i the initial volumetric soil moisture content. The source term $\mathbf{S_2}$ accounts for sediment entrainment and deposition processes, which are represented using the framework proposed (Hairsine & Rose, 1992a,

1992b). In particular,

$$\mathbf{S_2} = \begin{Bmatrix} 0 \\ 0 \\ 0 \\ e_1 + e_{r1} + r_1 + r_{r1} - d_1 \\ \vdots \\ e_k + e_{rk} + r_k + r_{rk} - d_k \end{Bmatrix}, \tag{11}$$

where e_k and e_{rk} are sediment detachment and re-detachment rates due to raindrop impact for sediment particles in size class k, r_k and r_{rk} are rates of entrainment and re-entrainment due to runoff, and d_k is the effective deposition rate. The model differentiates between original soil, which has not yet been entrained and transported during the modeled rainstorm, and deposited sediment, which has been detached and subsequently deposited. Detachment rates for entraining original sediment and re-entraining deposited sediment are computed differently. Sediment in the deposited layer may also fail en-masse (McGuire et al., 2017). Rates of sediment entrainment and re-entrainment by runoff are given by

$$r_k = (1 - H) p_k \frac{F(\Omega - \Omega_{cr})}{J}, \tag{12}$$

and

$$r_{rk} = H \frac{m_k}{m_t} \frac{F(\Omega - \Omega_{cr})}{\frac{\rho_s - \rho_f}{\rho_s} gh}. \tag{13}$$

Here, m_k is the deposited sediment mass per unit area for sediment in size class k, m_t is the total mass of deposited sediment per unit area, $H = \min(m_t/m_t^*, 1)$ accounts for the degree to which deposited sediment shields the underlying bed from erosion, m_t^* is the mass of deposited sediment needed to completely shield original sediment from erosion, ρ_f is the density of the flow, ρ_s is the density of sediment, F denotes the fraction of stream power effective in sediment entrainment, $\Omega = \rho_f g S_f \sqrt{uh^2 + vh^2}$ is stream power, and $S_f = \eta^2 (uh^2 + vh^2) h^{-10/3}$ is the friction slope. In this work, we consider a single particle size class characterized by a representative particle diameter, δ.

3.2 Rainfall and model parameters

A digital elevation model (DEM) of the study area is input to the Titan2D simulation. Here, we use a 1 m DEM derived from post-event airborne lidar. Elevations and slopes at locations required by the computational mesh are obtained using a 9 point (3× 3) finite difference stencil to interpolate on the DEM grid reducing the effects of arti-

283 facts and noise in the data (Patra et al., 2005). Errors in the DEM could be treated as
284 an uncertainty that is propagated through the simulation and subsequent analysis (Stefanescu,
285 Bursik, & Patra, 2012; Stefanescu, Bursik, Cordoba, et al., 2012), but we did not con-
286 sider this in the present study.

287 Runoff and debris flows initiated in the study area in response to a short duration,
288 high intensity burst of rainfall in the early morning hours of 9 January 2018 (Kean et
289 al., 2019). All simulations use 1-minute rainfall intensity data derived from the KTYD
290 rain gauge for a 20-minute time period that spans this short temporal window when rain-
291 fall intensity rapidly increased and debris flows initiated (Figure 2). The gauge is main-
292 tained by the Santa Barbara County Flood Control District and located approximately
5 km west of the San Ysidro Creek watershed.

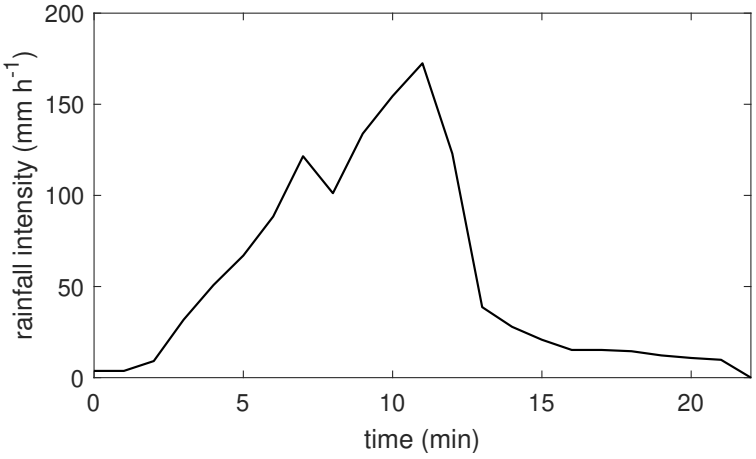

Figure 2. Rainfall hyetograph derived from the KTYD rain gauge, located roughly 5 km west of the San Ysidro Creek watershed.

293

294 Simulations were designed to explore the extent to which inundated area and peak
295 flow depths on the alluvial fan were influenced by rainfall intensity as well as several pa-
296 rameters that may play critical roles in debris-flow initiation and growth. We explored
297 the impact of different rainfall intensities by multiplying the 1-minute rainfall intensity
298 time series by a rainfall intensity factor ($\mathrm{RI_{fac}}$) that varied from 0.5 to 1.5. We also var-
299 ied the representative particle diameter, δ, from 0.05−0.125 mm, the fraction of stream
300 power effective in entrainment, F, from $0.001 - 0.006$, the hydraulic roughness coeffi-
301 cient, n_0, from $0.03 - 0.2$, and saturated hydraulic conductivity, k_s, from $5 - 25$ mm

302 h^{-1}. We further enforced a maximum soil thickness, r_{max}, that varied from 0.25−1.5
303 m to explore the role of sediment availability. All other parameters were fixed (Table 1,
304 Table 2). We used a Latin hypercube sampling strategy to generate 64 different param-
305 eter sets from the ranges specified above (McKay et al., 1979). Figure 3 shows the max-
306 imum flow depth for three of the 64 training simulations chosen to demonstrate typical
307 results with low, moderate, and long runout extents. Each of these simulations took sev-
308 eral hours to complete on an HPC cluster using up to 16 cores on an intel Xeon Gold
6226R processor.

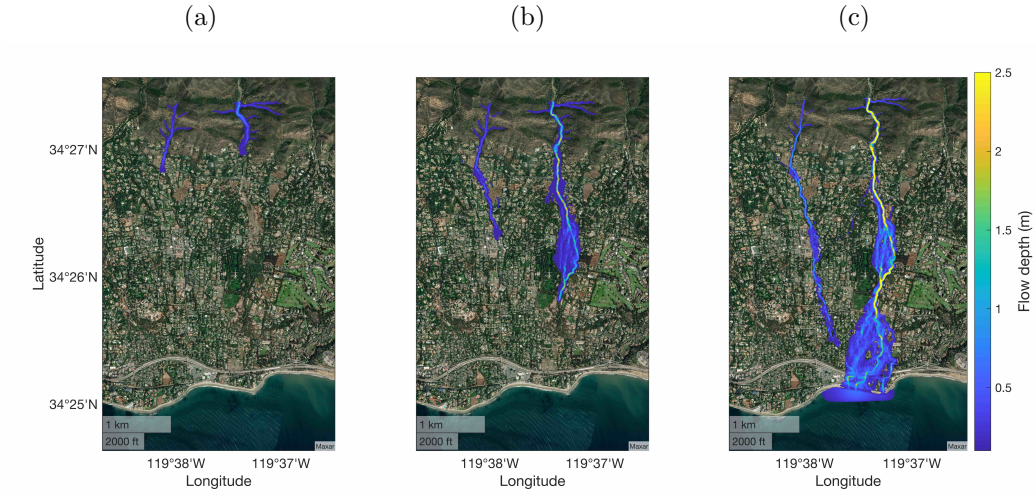

Figure 3. Maximum flow depth of three simulations resulting in (a) short runout (b) moderate runout and (c) long runout onto the alluvial fan. For contrast, the maximum colorbar limit is set to 2.5 m although maximum flow depth does exceed 2.5 m in some locations.

309

310 We chose to focus on exploring the effects of rainfall intensity, δ, F, n_0, k_s, and soil
311 thickness (sediment availability) since they control different aspects of the debris flow
312 initiation and growth process and, aside from rainfall intensity, they may all be strongly
313 affected by fire in our study area. Peak rainfall intensity over sub-hourly durations, par-
314 ticularly the 15-minute duration, is correlated well with runoff in recently burned wa-
315 tersheds in southern California (Kean et al., 2011). Peak 15-minute rainfall intensity is
316 also used in empirical models designed to predict postfire debris-flow likelihood and vol-
317 ume in the western USA (Staley et al., 2017; Gartner et al., 2014). We therefore expect
318 that variations in rainfall intensity during the relatively short (< 0.5 hours) portion of
319 the rainstorm that we are modeling will influence debris flow processes.

We expect the representative grain size, δ, to be relatively small in areas of concentrated flow immediately following fire in our study area given the propensity for postfire dry ravel to transport hillslope sediment to channels and valley bottoms (Florsheim et al., 1991; Lamb et al., 2011). Both δ and the amount of sediment available for transport, which we vary by enforcing a maximum soil thickness (r_{max}) throughout the model domain, may vary as a function of time since fire as sediment is exported from postfire rainstorms (Tang et al., 2019). Similarly, Liu et al. (2021) found that k_s and the Manning coefficient were lowest during rainstorms in the first year following a high severity fire in the San Gabriel Mountains, southern California, and increased by factors of roughly 3-4 over the next 4 years. Immediately following fire in southern California, values for the Manning coefficient and saturated hydraulic conductivity may be as low as $0.025-0.07$ s m$^{-1/3}$ and $1-6$ mm h^{-1}, respectively (Rengers et al., 2016; Tang et al., 2019; Liu et al., 2021). Kean et al. (2019) used post-event, point scale measurements with a tension infiltrometer to estimate the geometric mean of saturated hydraulic conductivity at 20 mm h^{-1} in the days following the Montecito debris flows. The effective fraction of stream power, F, may be expected to increase immediately following fire due to reductions in roughness associated with ground cover and vegetation. Past studies suggest values of $F \approx 0.005$ perform reasonably well in steep, recently burned watersheds in southern California (McGuire et al., 2017; Tang et al., 2019).

3.3 Emulating debris flows

Statistical emulators are effectively probabilistic models of computationally intensive physical model systems or *simulators*. That is, statistical emulators relate a set of user-defined inputs, often physical parameter specifications, to simulator output. Gaussian process emulators (GPs) are a popular class of surrogates for approximating and quantifying uncertainties in simulators as they (almost) interpolate computer model output (Sacks, Schiller, & Welch, 1989; Sacks, Welch, et al., 1989; Santner et al., 2003; Rasmussen & Williams, 2006). Further, the variance of the associated GP offers a quick mechanism to assess the uncertainty of using the emulator in place of the simulator for model prediction at untested inputs. Thus GP emulators offer a rapid and quantifiable mechanism to approximate output from physical process models that are computationally intensive to exercise. The parallel partial emulator (PPE) (Gu & Berger, 2016) extends this surrogate model to vector valued output.

Inputs to GP emulators are user defined. They are typically influential parameters, which show up within the governing dynamics, the forcing terms, or boundary conditions, as opposed to independent variables in the physical model. For the model described in Sec 3.1, we choose $p = 6$ parameters to define our input vector, namely those described in Sec 3.2 and given by $\mathbf{q} = [k_s, r_{max}, \eta_0, F, \delta, RI_{\text{fac}}]$. The rainfall intensity factor is a scaling of the true rainfall time series that triggered the debris flows in our study area.

In initial explorations, the ratio of pore fluid pressure to total basal normal stress, λ, was also considered, but found to not substantially influence spatial patterns in peak flow depth and runout extent on the fan. We will discuss the relationship between GP emulators and sensitivity analysis further in Sec 4. The output under consideration, $\mathbf{y}$, is the maximum (over time) flow depth at each of $s = 1.4M$ map points. The main objective of the emulator is to predict the output of the Titan2D model at an untested scenario, $\mathbf{q}^*$, given a relatively modest set of N training or *design* runs $\mathbf{q}^{\text{D}}$ and each of their corresponding inundation depth outputs, $\mathbf{y}_j^{\text{D}}$, $j = 1, \ldots, N$. In this work, we take $N = 64$ training runs and each output vector, $\mathbf{y}_j^{\text{D}}$, is a $1.4M$ element vector recording the peak flow depth at each map point. Collecting these outputs together, we have Y^{D}, as a $64 \times 1.4M$ matrix of training run outputs. The 64 training run inputs are chosen by a Latin hypercube design (McKay et al., 1979; Santner et al., 2003) covering the ranges of inputs listed in Table 1. All other parameters are fixed (Table 2). To fit the emulator, these parameter ranges are normalized to a unit hypercube.

Given the training data, $\{\mathbf{q}^{\text{D}}, Y^{\text{D}}\}$, to approximate the inundation resulting from an untested scenario, $\mathbf{q}^*$, we use the predictive mean of the PPE given by

$$\tilde{\mathbf{y}}(\mathbf{q}^*) = \mathbf{h}^{\text{T}}(\mathbf{q}^*)B + \mathbf{r}^{\text{T}}(\mathbf{q}^*)R^{-1}(Y^{\text{D}} - H^{\text{D}}B), \tag{14}$$

where R is an $N \times N$ (64×64 in this work) matrix of correlations between pairs of design inputs, $\mathbf{r}(\mathbf{q}^*)$ is an $N \times 1$ vector of correlations between the untested input, $\mathbf{q}^*$, and each of the input scenarios in the design, $\mathbf{q}^{\text{D}}$. Further, $\mathbf{h}(\mathbf{q})$ is a $l \times 1$ vector of regression variables, often taken to be constant or linear in $\mathbf{q}$ (i.e., $l = 1$ for constant case used in this work and $l = p + 1$ for the linear case), and H^{D} is and $N \times l$ matrix where the j^{th} row are the regression variables evaluated at the j^{th} design point, $\mathbf{h}^{\text{T}}(\mathbf{q}_j^{\text{D}})$. The matrix B is a $l \times s$ matrix of regression coefficients. Here, each of the $s = 1.4M$ outputs has its own set of regression coefficients, but a shared correlation structure. We use a

Model parameter	Min value	Max value	Range parameter
k_s: Saturated hydraulic conductivity (mm h^{-1})	5	20	3.5
r_{max}: Maximum soil thickness (m)	0.25	1.5	9.9
η_0: hydraulic roughness coefficient (s $m^{-1/3}$)	0.03	0.2	0.15
F: Fraction of stream power effective in sediment detachment	0.6×10^{-3}	1.0×10^{-3}	9.9
δ: Effective grain size (mm)	0.05	0.125	5.8
RI_{fac}: Rainfall intensity factor	0.5	1.5	0.38

Table 1. Parameter ranges with units and GP range parameters (unit-less) for the six parameters that varied among the N=64 debris flow simulations.

Matérn 5/2 correlation function (Stein, 1999). For two scenarios, e.g., two input points $\mathbf{q}_i = (x_{i1}, \ldots, x_{ip})^{\mathrm{T}}$ and $\mathbf{q}_j = (x_{j1}, \ldots, x_{jp})^{\mathrm{T}}$, the standardized distance and correlation between these input scenarios are given by

$$d_k = \Big(\frac{|x_{ik} - x_{jk}|^2}{\theta_k^2}\Big)^{1/2}, \qquad k = 1, \ldots, p$$
$$c(\mathbf{q}_i, \mathbf{q}_j) = \prod_{k=1}^{p} \Big(1 + \sqrt{5}d_k + \frac{5}{3}d_k^2\Big) \exp\big(-\sqrt{5}d_k\big), \tag{15}$$

respectively. The predictive variance for each output dimension (pixel) of the PPE is given by

$$\mathbf{v}_j(\mathbf{q}^*) = \sigma_j^2 \Big(1 - \mathbf{r}^{\mathrm{T}}(\mathbf{q}^*) R^{-1} \mathbf{r}(\mathbf{q}^*) + \big(\mathbf{h}(\mathbf{q}^*) - (H^{\mathrm{D}})^{\mathrm{T}} R^{-1} \mathbf{r}(\mathbf{q}^*)\big)^{\mathrm{T}} \times \big((H^{\mathrm{D}})^{\mathrm{T}} R^{-1} H^{\mathrm{D}}\big)^{-1} \big(\mathbf{h}(\mathbf{q}^*) - (H^{\mathrm{D}})^{\mathrm{T}} R^{-1} \mathbf{r}(\mathbf{q}^*)\big)\Big), \tag{16}$$

where σ_j^2, $(j = 1, \ldots, s)$ is the scalar variance corresponding to each pixel's output. "Fitting" a PPE amounts to estimating the regression parameters in B, the scalar variances at of each output, σ_j^2, and the *range parameters* $\{\theta_k : k = 1, \ldots, p\}$. To do so, we use the `RobustGaSP` package (Gu et al., 2018, 2019). On a laptop, fitting a PPE to $1.4M$ pixels of output with $N = 64$ training runs takes roughly 10 minutes.

GP emulators have been applied to Titan2D-based volcanic debris flows (Bayarri et al., 2009, 2015; Spiller et al., 2014; Rutarindwa et al., 2019) and recently to other Titan2D-based debris flows (Zhao et al., 2021; Zhao & Kowalski, 2022). In each of these studies,

Table 2. Model parameters using the same notation as (McGuire et al., 2017).

Symbol	Definition	Value	Unit
a_0	Detachability of original soil	1000	kg m^{-2} s^{-1}
a_{d0}	Detachability of deposited sediment	2000	kg m^{-2} s^{-1}
m^*_{t0}	Deposited sediment needed to shield original soil	2.7	kg m^{-2}
J	Specific energy of entrainment	15.125	m^2 s^{-2}
C	Effective cohesion	200	Pa
ϕ_{bed}	Basal friction angle	32	deg
λ	Ratio of pore fluid pressure to total normal stress	0.8	-
C_v	Fraction vegetation cover	0	-
h_f	Wetting front poential	1	mm
θ_i	Initial volumetric soil moisture	0.1	-
θ_s	Volumetric soil moisture at saturation	0.39	-
ϵ	Exponent in friction model	0.33	-
h_c	Critical depth in friction model	3	mm

source terms (particularly debris mass or flux) were specified via ad-hoc parameterizations which are less appropriate for postfire, runoff-generated debris flows.

3.4 Numerical Experiments

Evaluation of the GP emulator's mean quickly allows one to explore any output quantity of interest over the parameter space. Here we take the output quantity of interest, $\mathbf{y}$, to be the maximum debris-flow depth at all locations. Additionally, the variance of the GP emulator accounts for the uncertainty introduced by evaluating the GP mean, $\tilde{\mathbf{y}}$, instead of the debris-flow process model. We can break our exploration of numerical experiments into three groups.

First, we perform leave-one-out experiments as a test of the PPE performance. This experiment amounts to excluding one simulation at a time, fitting a GP to the 63 remaining simulations, and then comparing the GP predicted inundation of the left-out scenario to actual simulated inundation for that scenario. This is repeated for each of the $N = 64$ simulations.

Second, we explore the relative importance of different model parameters using the GP's range parameters. The range parameters are positive numbers indicating the influence of each model parameter on the model response – the smaller the range parameter, the more influence the corresponding model parameter has on the debris flow model (i.e. maximum flow depth). As such, these range parameters act as an effective sensitivity analysis.

Lastly, we employ the emulator to isolate and explore how flow extent/depths are driven by (1) changes in rainfall intensity and (2) changes in saturated hydraulic conductivity and hydraulic roughness that occur as the landscape recovers. We focus, in particular, on exploring the effects of postfire changes in saturated hydraulic conductivity and hydraulic roughness since Liu et al. (2021) provide guidance for parameterizing these effects in the nearby San Gabriel Mountains. Since the GP emulator enables rapid forward uncertainty quantification, we demonstrate how it can be used to accelerate a Monte Carlo probability of inundation calculation for two cases, namely when the observed storm occurs 2 months and 14 months postfire.

4 Results

4.1 Emulator performance

To test the performance of the GP emulator for approximating the Titan2D simulations, we examine leave-one-out predictions. Of note, the range parameter estimates were very stable. We found the coefficients of variation for each of the six values to be between 0.01-0.10 indicating that the relative influence of any input to the GP was not swayed strongly by any single flow simulation. For illustrative purposes, we focus on two points of interest – one located in a channel and one on the adjacent fan surface where flow is relatively unconfined. In Figure 4 for both cases we sort the simulations by their left-out flow depths, $\mathbf{y}$, and predict each with a credible interval centered at the mean of the GP, $\tilde{y}$. We find root mean squared errors from these leave-one-out experiments of 0.12m and 0.17m for the locations on the fan and on the channel, respectively. Further, we see that 89% (fan location) and 94% (channel location) of the simulated depths fall within their predictive credible intervals. These numbers are slightly below the anticipated 95%, but this is likely due to the relatively small training set, and in the case

447 of the fan location, the fact that roughly half of the simulations resulted in no inunda-
tion, which is challenging for GP emulation (Spiller et al., 2023).

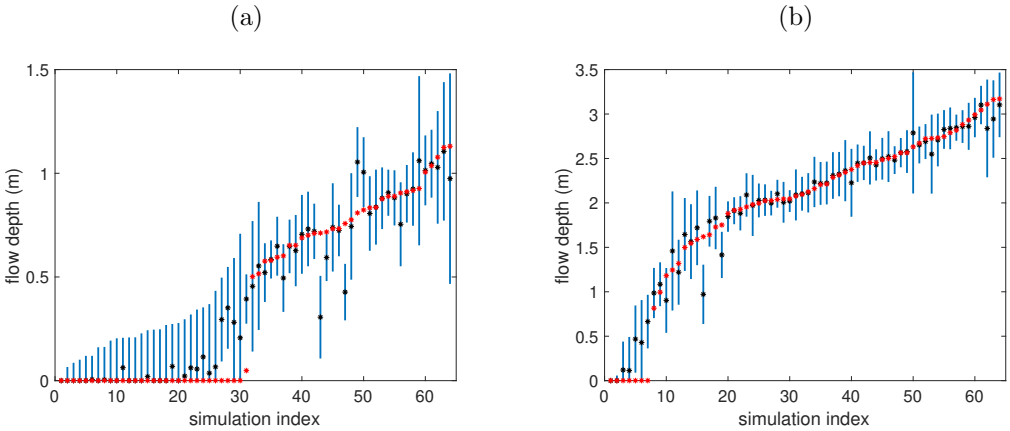

Figure 4. Leave-one-out experiments for (a) a location on the fan and (b) a location in the channel (see Figure 7 for details). In each panel, indices are sorted based on the simulated max flow depth (red stars). GP predictive means for these scenarios are plotted in black while the 95% credible intervals are plotted as vertical blue bars.

448

449 ### 4.2 Sensitivity analysis

450 A crucial step to fitting a GP is estimating the range parameters. Smaller range
451 parameters indicate that the corresponding model parameter has more influence on the
452 debris flow model output of interest (i.e. maximum flow depth). From table 1, one can
453 see that the debris flow model is most sensitive to rainfall intensity and the hydraulic
454 roughness coefficient; it is moderately sensitive to saturated hydraulic conductivity and
455 effective grain size; and is relatively insensitive to the maximum soil thickness and to the
456 fraction of stream power effective in sediment detachment.

457 Scaling the rainfall intensity time series has a substantial effect on inundation ex-
458 tent (Figure 5). As the rainfall leading to the flows after the Thomas fire were quite in-
459 tense, it is not surprising to see significant runout even when $RI_{fac} = 0.5$, though the
460 extent of inundation is diminished relative to cases with more intense rainfall, namely
461 $RI_{fac} = 1$ and $RI_{fac} = 1.5$. More intense rainfall leads to both increased water runoff
462 and sediment entrainment, leading to greater flow volumes and increases in peak flow
463 depth and area inundated.

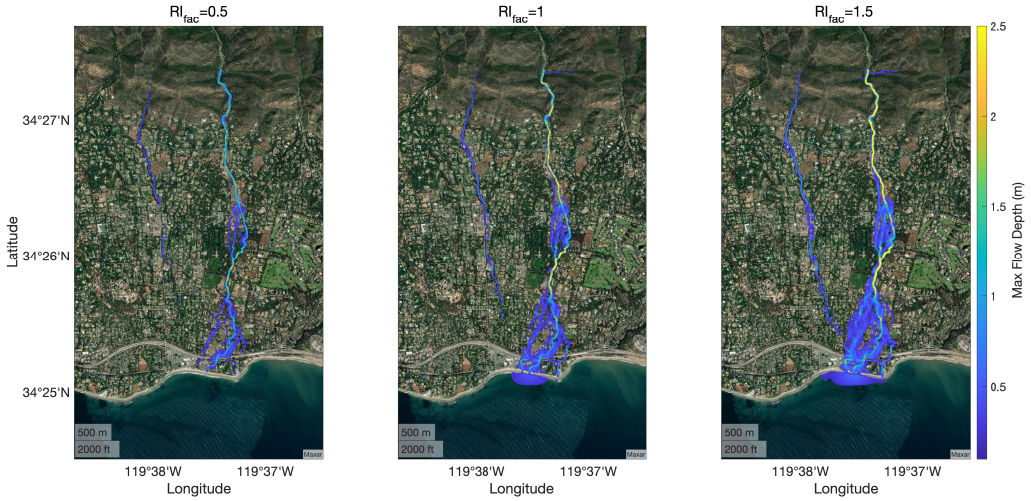

Figure 5. Maximum flow depth for 50% (RI_{fac}=0.5), 100% (RI_{fac}=1), and 150% (RI_{fac}=1.5) scaling of the rainfall time series. Other parameters are set at their nominal value, except for hydraulic roughness and saturated hydraulic conductivity which were set to the minimal values in table 1, consistent with values anticipated immediately after the fire. For contrast, the maximum colorbar limit is set to 2.5 m although in the channels towards the north, maximum flow depth exceeds 2.5m.

4.3 Effects of postfire recovery on runout

Liu et al. (2021) developed parametric best-fit curves to model the change in saturated hydraulic conductivity and hydraulic roughness as a function of time following fire in the nearby San Gabriel Mountains. Using these relationships, and setting others to the center of their respective ranges, we use the GP emulator to explore the effects of temporal changes in the hydraulic roughness coefficient and saturated hydraulic conductivity. Both peak flow depth and area inundated in response to the observed rainstorm would decrease substantially over the first six months following fire (Figure 6). For example, US Highway 101, which runs perpendicular to the direction of flow near the distal portion of the fan, would only be inundated when the rainstorm occurs within the first 3 months following fire. If the observed rainstorm were to have occurred 12 months following the fire, the simulated inundation area would be limited to channels near the fan apex.

We can also explore the effects of rainfall intensity and temporal changes in hydraulic roughness and saturated hydraulic conductivity following fire by examining flow depth

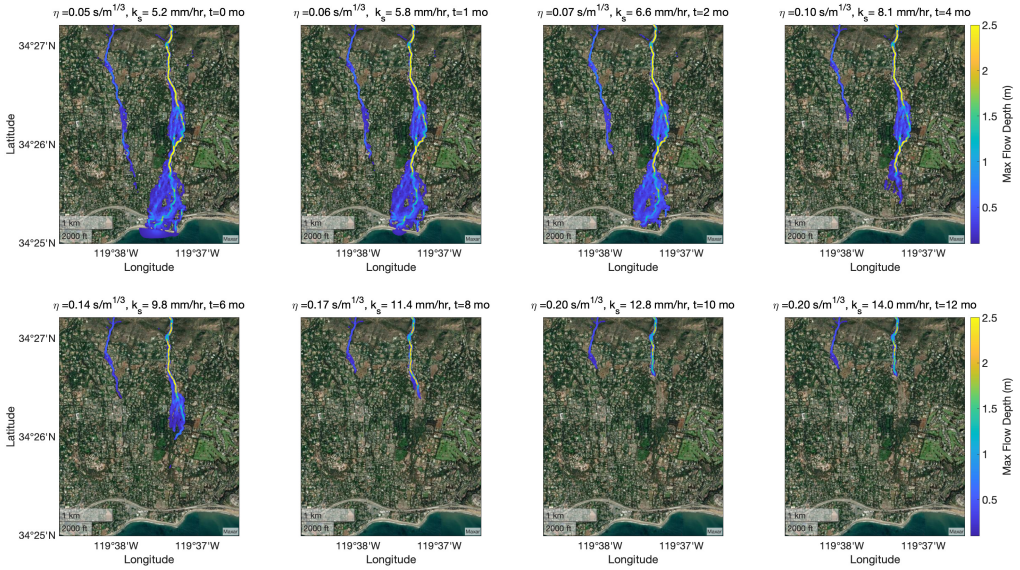

Figure 6. Maximum inundation for several values of the Manning coefficient and saturated hydraulic conductivity along with the corresponding time from Figures 7b and 7c of Liu et al. (2021), respectively. All of the other parameters are set to the center value of their range. For contrast, the max colorbar limit is set to 2.5 m although in the channels towards the north, max flow depth exceeds 2.5m.

at distinct points of interest. Again, we consider the same two points for illustrative purposes, one located in a channel and one on the adjacent fan surface where flow is relatively unconfined (Figure 7). For a given time since fire, peak flow depths are greater in the channel relative to on the fan surface, as expected. Peak flow depth decreases gradually over the first several months at the point on the fan before dropping to near zero after approximately six months. Peak flow depths decrease over the first year following fire in the channel location from roughly 2.5 m to 1.5 m. Visualizing peak flow depths as a function of time since fire and rainfall intensity can be helpful for assessing temporal shifts in the magnitude of rainfall associated with potential debris-flow impacts at different locations. For example, even a rainstorm characterized by $RI_{fac} = 1.5$ would not result in peak flow depths greater than 20 cm after approximately 0.6 years following fire.

We further use the emulator to produce probabilistic maps of inundation at different times following fire (Figure 8). Differences in the spatial patterns of inundation

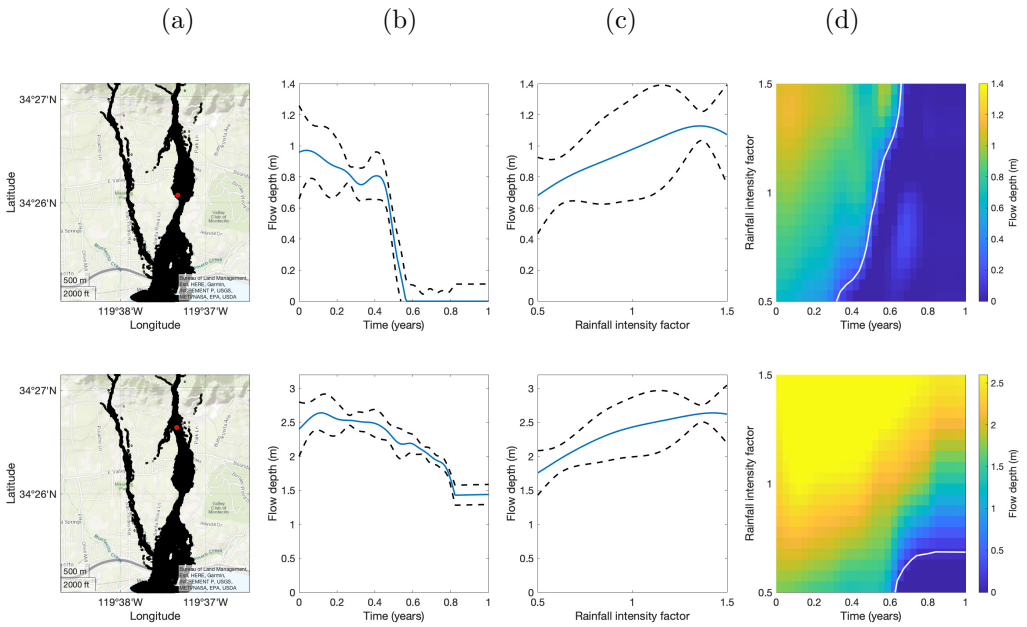

Figure 7. Exploration at one location on the fan (top row) and one location in the channel (bottom row). Panels in column (a) indicate locations of all emulated flow depths (black) and those being explored in detail (red). Panels in column (b) show peak flow depth as a function of time since fire. The hydraulic roughness coefficient and saturated hydraulic conductivity are parameterized as a function of time since (Liu et al., 2021) while all other parameters set at their central values. (Note that the vertical scales are different; the maximum flow depth on the fan is roughly 1.0 m, and that in the channel is roughly 2.5 m.) Panels in column (c) show peak flow depth versus rainfall intensity with the hydraulic roughness coefficient and saturated hydraulic conductivity set to their respectively minimum values (i.e. as would be expected prior to any recovery) and with all other parameters set at their central values. Panels in column (d) contain color maps for maximum flow depth at these two locations varying all combinations of rainfall intensity and time (via Manning coefficient and saturated hydraulic conductivity). The white contours indicate the values of time and rainfall intensity leading to an inundation of 10 cm or more.

493 likelihood are apparent between scenarios where the storm occurs 2 months following the
494 fire versus 14 months. We identify a location as being inundated if peak flow depth ex-
495 ceeds $> 0.1m$. All parameters were set to their central values except for saturated hy-
496 draulic conductivity and the hydraulic roughness coefficient. The latter parameter is sam-
497 pled from the distribution suggested by Liu et al. (2021) while the former is set to 2 and
498 14 month values, respectively, estimated from the same study. The probability MC cal-
culation was carried out with 100 samples.

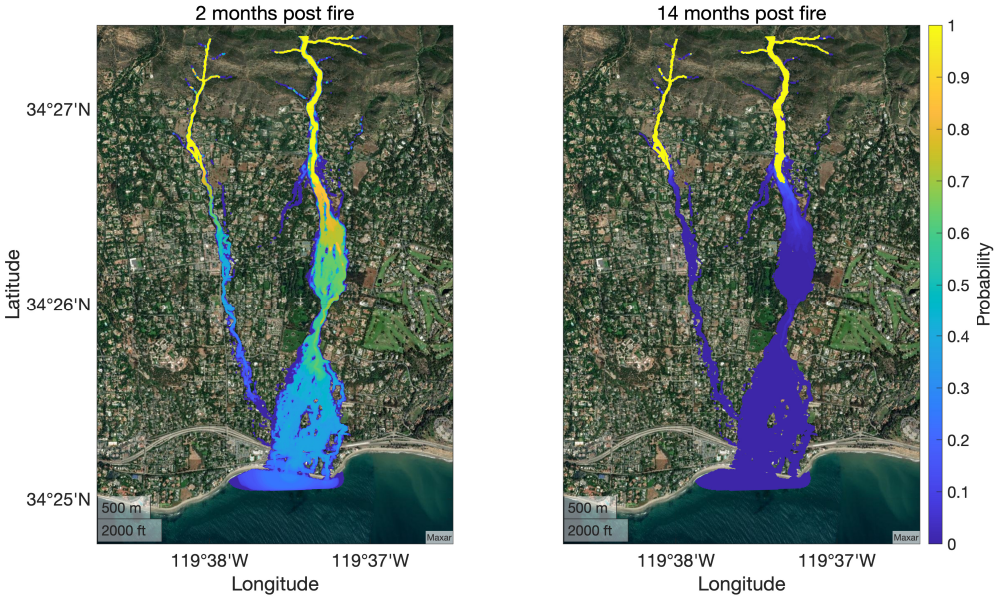

Figure 8. Probability of inundation maps, where a location is considered inundated if the maximum flow depth exceeds 10 cm. To calculate this probability, all parameters except the Manning coefficient and saturated hydraulic conductivity are set to their central values with the latter set to values corresponding to the 2 month and 14 month estimates from Liu et al. (2021), respectively.

499

500 5 Discussion

501 Fire impacts on soil and vegetation properties that affect the initiation and growth
502 of runoff-generated debris flows are most extreme in the first few months following fire
503 (DeGraff et al., 2015; Thomas et al., 2021). Potentially rapid changes in hydrologic con-
504 ditions following fire limit the time window for gathering data needed to constrain pa-

rameters for postfire runoff and erosion models, including the model used here. Aside from rainfall intensity, which will not be affected by the fire, we found that hydraulic roughness, the representative grain size, and saturated hydraulic conductivity played the most important roles in controlling debris flow inundation. Additional model testing across fire-prone regions in different geologic and climate settings is needed to assess model performance and determine the extent to which results related to parameter sensitivity are generalizable. Nonetheless, this result provides observational targets that can help focus future efforts to collect perishable postfire data.

We hypothesize that hydraulic roughness plays an important role in controlling inundated area and peak flow depths because of its influence on both modeled sediment detachment rates and flow resistance. Saturated hydraulic conductivity will influence the rate at which sediment is detached by overland flow since it exerts a strong control on the magnitude of infiltration-excess overland flow that often dominates in postfire settings. Increased rates of sediment detachment lead to increases in flow volume, which in turn acts to increase runout and inundation potential (Barnhart et al., 2021). Grain size similarly influences flow volume since a larger grain size will encourage more rapid deposition of sediment.

Our evaluation of parameter sensitivity indicates that constraints on postfire values for hydraulic roughness, saturated hydraulic conductivity, and the grain size distribution of sediment entrained in debris flows would be particularly beneficial for improving estimates of debris flow runout estimates. Burn severity is likely to play a substantial role in a fire's effect on these variables (Moody et al., 2015; McGuire & Youberg, 2020). In addition, attempts to capture changes in debris flow runout as a function of time since fire would benefit from methods to parameterize temporal changes in hydraulic roughness, saturated hydraulic conductivity, and the grain size distribution of sediment entrained in debris flows. Fire-driven reductions in hydraulic roughness are commonly cited as a cause for increased runoff and erosion (McGuire & Youberg, 2020; Stoof et al., 2015), but there are few constraints on the temporal changes in hydraulic roughness following fire, which may be facilitated by changes in vegetation cover and/or grain roughness. Particularly in southern California (Doehring, 1968; Florsheim et al., 1991; DiBiase & Lamb, 2020) and other tectonically active regions in the western USA (Roering & Gerber, 2005), fire can promote substantial increases in dry ravel activity on hillslopes that may reduce hydraulic roughness by increasing the availability of fine sediment in channels. Hydraulic

roughness may then increase over time as dry ravel deposits are progressively eroded during postfire rainstorms (Tang et al., 2019). Temporal changes in debris flow sediment source locations (Guilinger et al., 2020) and coarsening of particle size distributions due to preferential erosion of fines would also influence the effective grain size in the model. In practice, it is not clear how to quantitatively connect this single grain size parameter to the particle size distribution of hillslope or channel sediment, especially when flows contain boulders. Postfire changes in saturated hydraulic conductivity can be inferred from calibration of hydrologic models (Liu et al., 2021), rainfall simulator experiments at the small plot scale (Robichaud et al., 2016), and point scale measurements (Ebel, 2020; Ebel et al., 2022; Perkins et al., 2022). While some general patterns have been observed between time since fire and values of saturated hydraulic conductivity, there is substantial site-to-site variability (Ebel & Martin, 2017). The level of uncertainty in influential model input parameters and how they change over time highlights the need for probabilistic assessments of debris flow runout, which emulators can help to achieve by facilitating rapid exploration of large parameter spaces.

Rainfall is a necessary driver for debris flow initiation and the model was also sensitive to rainfall intensity, specifically a rainfall intensity factor which we used to scale the rainfall intensity time series. This finding is consistent with observations that postfire basin-scale sediment yields (Pak & Lee, 2008) and debris flow volume (Gartner et al., 2014) increase with rainfall intensity averaged over durations of 60 minutes or less. Short duration (sub-hourly) bursts of high intensity rainfall are effective at generating infiltration-excess overland flow that can trigger debris flows in recently burned steeplands (Kean et al., 2011; Nyman et al., 2011; Esposito et al., 2023). Emulators may be useful for generating probabilistic maps of debris flow inundation in response to design storms with different rainfall intensities or examining changes at particular points of interest. In cases where there are specific values at risk downstream of a burned area, rapid exploration of debris flow characteristics (i.e. peak flow depth) as a function of rainfall intensity could help define impact-based rainfall thresholds that could be used for planning and warning purposes. In other words, one could take advantage of the emulator's computational efficiency to determine, not only the rainfall intensity required to initiate a debris flow but also the rainfall intensity required to produce a debris flow that would impact a prescribed area of interest with some prescribed depth of flow.

The computational cost of many physically-based debris flow models is a limitation in applications that are time sensitive, such as rapid postfire hazard assessments. Postfire debris flows in the western USA, such as those that occurred near Montecito, may occur before the fire has been officially contained and within weeks or months of fire ignition. The emulator methodology presented here provides one avenue for minimizing computation times, since an initial suite of simulations can be used to train the emulator which can later be applied with substantially less computational effort to generate a probabilistic hazard map for a specific scenario. An emulator may even be trained prior to a fire. Analogous approaches have been employed in related applications (Rutarindwa et al., 2019; Spiller et al., 2020). Within the context of postfire hazards, an emulator could be used to assess debris-flow runout and inundation downstream of a burned area in response to a design or forecast rainstorm. Atmospheric model ensembles, for example, can provide estimates of peak 15-minute rainfall intensity over watersheds of interest that could be used to constrain a distribution of rainfall intensity factors (Oakley et al., 2023).

6 Conclusions

We develop a physics based high fidelity computationally expensive morphodynamic model and cost effective surrogates based on Gaussian process models of postfire debris flows. We employ the Gaussian Process surrogate model, or emulator, to approximate peak debris flow depth from a physics-based morphodynamic model, Titan2D. The emulator is able to approximate the peak flow depth with a mean squared error that is generally in the range of $0.1-0.2$ m when using a modest training data set built from 64 Titan2D simulations. The range parameters associated with the emulator provide a metric for the relative importance of input parameters, which provides guidance for those that are most important to constrain for forward modeling of debris flow runout. We find that peak flow depths are most sensitive to changes in hydraulic roughness and a rainfall intensity factor and are moderately sensitive to saturated hydraulic conductivity and effective grain size. We highlight the emulator's ability to provide rapid estimates of peak flow depth for parameter combinations that were not part of the training data set by generating probabilistic maps of inundation as a function of time since fire. Inundation likelihood changes substantially over the first year following the fire, driven by temporal variations in hydraulic roughness and saturated hydraulic conductivity. Emulator-based analyses can facilitate rapid Monte Carlo calculations of inundation probability, making them

a promising option for rapid postfire hazard assessments and scenario planning before a fire starts.

Data Availability Statement

The debris flow model under consideration in this paper is from (McGuire et al., 2017) and it is accelerated by implementation in the Titan2D platform (Patra et al., 2005; Simakov et al., 2019). Parametric models of the Manning coefficient and saturated hydraulic conductivity versus time are available from (Liu et al., 2021) as are validated samples of those same parameters for debris flows 2 and 14 months post fire. Packages to implement the parallel partial emulator (Gu & Berger, 2016) are available in (Gu et al., 2019).

Acknowledgments

Spiller was supported by the National Science Foundation grant DMS-2053872 and Marquette University's Way Klingler Fellowship. McGuire was supported through the California Department of Water Resources Atmospheric River Program (4600013361). Patra and Patel were supported by the National Science Foundation grant OAC-2004302. Pitman was supported by the National Science Foundation grant DMS-2053874.

References

Alessio, P., Dunne, T., & Morell, K. (2021). Post-wildfire generation of debris-flow slurry by rill erosion on colluvial hillslopes. *Journal of Geophysical Research: Earth Surface*, *126*(11), e2021JF006108.

Barnhart, K. R., Jones, R. P., George, D. L., McArdell, B. W., Rengers, F. K., Staley, D. M., & Kean, J. W. (2021). Multi-model comparison of computed debris flow runout for the 9 january 2018 montecito, california post-wildfire event. *Journal of Geophysical Research: Earth Surface*, *126*(12), e2021JF006245.

Bayarri, M. J., Berger, J. O., Calder, E. S., Dalbey, K., Lunagómez, S., Patra, A. K., ... Wolpert, R. L. (2009). Using statistical and computer models to quantify volcanic hazards. *Technometrics*, *51*(4), 402–413. doi: 10.1198/TECH.2009.08018

Bayarri, M. J., Berger, J. O., Calder, E. S., Patra, A. K., Pitman, E. B., Spiller, E. T., & Wolpert, R. L. (2015). A methodology for quantifying volcanic haz-

ards. *International Journal of Uncertainty Quantification*, *5*(4), 297–325. doi: 10.1615/Int.J.UncertaintyQuantification.2015011451

Conedera, M., Peter, L., Marxer, P., Forster, F., Rickenmann, D., & Re, L. (2003). Consequences of forest fires on the hydrogeological response of mountain catchments: a case study of the riale buffaga, ticino, switzerland. *Earth Surface Processes and Landforms: The Journal of the British Geomorphological Research Group*, *28*(2), 117–129.

Currin, C., Mitchell, T., Morris, M., & Ylvisaker, D. (1988). *A Bayesian approach to the design and analysis of computer experiments* (Tech. Rep.). Oak Ridge, TN (USA): Oak Ridge National Laboratory. Retrieved from `https://www.osti.gov/biblio/6734087`

Dalbey, K., Patra, A. ., Pitman, E. B., Bursik, M. I., & Sheridan, M. F. (2008). Input uncertainty propagation methods and hazard mapping of geophysical mass flows. *Journal of Geophysical Research: Solid Earth*, *113*(B5), 1–16. doi: 10.1029/2006JB004471

DeGraff, J. V., Cannon, S. H., & Gartner, J. E. (2015). The timing of susceptibility to post-fire debris flows in the western united states. *Environmental & Engineering Geoscience*, *21*(4), 277–292.

Diakakis, M., Mavroulis, S., Vassilakis, E., & Chalvatzi, V. (2023). Exploring the application of a debris flow likelihood regression model in mediterranean post-fire environments, using field observations-based validation. *Land*, *12*(3), 555.

DiBiase, R. A., & Lamb, M. P. (2020). Dry sediment loading of headwater channels fuels post-wildfire debris flows in bedrock landscapes. *Geology*, *48*(2), 189–193.

Doehring, D. O. (1968). The effect of fire on geomorphic processes in the san gabriel mountains, california. *Rocky Mountain Geology*, *7*(1), 43–65.

Ebel, B. A. (2020). Temporal evolution of measured and simulated infiltration following wildfire in the colorado front range, usa: Shifting thresholds of runoff generation and hydrologic hazards. *Journal of Hydrology*, *585*, 124765.

Ebel, B. A., & Martin, D. A. (2017). Meta-analysis of field-saturated hydraulic conductivity recovery following wildland fire: Applications for hydrologic model parameterization and resilience assessment. *Hydrological Processes*, *31*(21), 3682–3696.

Ebel, B. A., Moody, J. A., & Martin, D. A. (2022). Post-fire temporal trends in soil-physical and-hydraulic properties and simulated runoff generation: Insights from different burn severities in the 2013 black forest fire, co, usa. *Science of the Total Environment*, *802*, 149847.

Esposito, G., Gariano, S. L., Masi, R., Alfano, S., & Giannatiempo, G. (2023). Rainfall conditions leading to runoff-initiated post-fire debris flows in campania, southern italy. *Geomorphology*, *423*, 108557.

Florsheim, J. L., Keller, E. A., & Best, D. W. (1991). Fluvial sediment transport in response to moderate storm flows following chaparral wildfire, ventura county, southern california. *Geological Society of America Bulletin*, *103*(4), 504–511.

Gabet, E. J., & Bookter, A. (2008). A morphometric analysis of gullies scoured by post-fire progressively bulked debris flows in southwest montana, usa. *Geomorphology*, *96*(3-4), 298–309.

Gartner, J. E., Cannon, S. H., & Santi, P. M. (2014). Empirical models for predicting volumes of sediment deposited by debris flows and sediment-laden floods in the transverse ranges of southern california. *Engineering Geology*, *176*, 45–56.

Gibson, S., Moura, L. Z., Ackerman, C., Ortman, N., Amorim, R., Floyd, I., ... Sánchez, A. (2022). Prototype scale evaluation of non-newtonian algorithms in hec-ras: Mud and debris flow case studies of santa barbara and brumadinho. *Geosciences*, *12*(3), 134.

Gorr, A. N., McGuire, L. A., Youberg, A. M., & Rengers, F. K. (2022). A progressive flow-routing model for rapid assessment of debris-flow inundation. *Landslides*, *19*(9), 2055–2073.

Graber, A. P., Thomas, M. A., & Kean, J. W. (2023). How long do runoff-generated debris-flow hazards persist after wildfire? *Geophysical Research Letters*, *50*(19), e2023GL105101.

Gu, M., & Berger, J. O. (2016). Parallel partial Gaussian process emulation for computer models with massive output. *The Annals of Applied Statistics*, *10*(3), 1317–1347. doi: 10.1214/16-AOAS934

Gu, M., Palomo, J., & Berger, J. O. (2019). RobustGaSP: Robust Gaussian Stochastic Process Emulation in R. *The R Journal*, *11*(1), 112–136. Retrieved from `https://doi.org/10.32614/RJ-2019-011` doi: 10.32614/RJ-2019-011

Gu, M., Wang, X., & Berger, J. O. (2018). Robust gaussian stochastic process

emulation. *The Annals of Statistics*, *46*(6A), 3038–3066. doi: 10.1214/17-AOS1648

Guilinger, J. J., Gray, A. B., Barth, N. C., & Fong, B. T. (2020). The evolution of sediment sources over a sequence of postfire sediment-laden flows revealed through repeat high-resolution change detection. *Journal of Geophysical Research: Earth Surface*, *125*(10), e2020JF005527.

Hairsine, P., & Rose, C. (1992a). Modeling water erosion due to overland flow using physical principles: 1. sheet flow. *Water resources research*, *28*(1), 237–243.

Hairsine, P., & Rose, C. (1992b). Modeling water erosion due to overland flow using physical principles: 2. rill flow. *Water resources research*, *28*(1), 245–250.

Hoch, O. J., McGuire, L. A., Youberg, A. M., & Rengers, F. K. (2021). Hydrogeomorphic recovery and temporal changes in rainfall thresholds for debris flows following wildfire. *Journal of Geophysical Research: Earth Surface*, *126*(12), e2021JF006374.

Iverson, R. M., Reid, M. E., & LaHusen, R. G. (1997). Debris-flow mobilization from landslides. *Annual Review of Earth and Planetary Sciences*, *25*(1), 85–138.

Kean, J. W., Staley, D. M., & Cannon, S. H. (2011). In situ measurements of post-fire debris flows in southern california: Comparisons of the timing and magnitude of 24 debris-flow events with rainfall and soil moisture conditions. *Journal of Geophysical Research: Earth Surface*, *116*(F4).

Kean, J. W., Staley, D. M., Lancaster, J. T., Rengers, F. K., Swanson, B. J., Coe, J. A., ... Lindsay, D. N. (2019). Inundation, flow dynamics, and damage in the 9 january 2018 montecito debris-flow event, california, usa: Opportunities and challenges for post-wildfire risk assessment. *Geosphere*, *15*(4), 1140–1163.

Kinnell, P. (2005). Raindrop-impact-induced erosion processes and prediction: a review. *Hydrological Processes: An International Journal*, *19*(14), 2815–2844.

Lamb, M. P., Scheingross, J. S., Amidon, W. H., Swanson, E., & Limaye, A. (2011). A model for fire-induced sediment yield by dry ravel in steep landscapes. *Journal of Geophysical Research: Earth Surface*, *116*(F3).

Lancaster, J. T., Swanson, B. J., Lukashov, S. G., Oakley, N. S., Lee, J. B., Spangler, E. R., ... others (2021). Observations and analyses of the 9 january 2018 debris-flow disaster, santa barbara county, california. *Environmental &*

Engineering Geoscience, *27*(1), 3–27.

Liu, T., McGuire, L. A., Wei, H., Rengers, F. K., Gupta, H., Ji, L., & Goodrich, D. C. (2021). The timing and magnitude of changes to hortonian overland flow at the watershed scale during the post-fire recovery process. *Hydrological Processes*, *35*(5), e14208.

McGuire, L. A., Kean, J. W., Staley, D. M., Rengers, F. K., & Wasklewicz, T. A. (2016). Constraining the relative importance of raindrop-and flow-driven sediment transport mechanisms in postwildfire environments and implications for recovery time scales. *Journal of Geophysical Research: Earth Surface*, *121*(11), 2211–2237.

McGuire, L. A., Rengers, F. K., Kean, J. W., & Staley, D. M. (2017). Debris flow initiation by runoff in a recently burned basin: Is grain-by-grain sediment bulking or en masse failure to blame? *Geophysical Research Letters*, *44*(14), 7310–7319.

McGuire, L. A., Rengers, F. K., Oakley, N., Kean, J. W., Staley, D. M., Tang, H., ... Youberg, A. M. (2021). Time since burning and rainfall characteristics impact post-fire debris-flow initiation and magnitude. *Environmental & Engineering Geoscience*, *27*(1), 43–56.

McGuire, L. A., & Youberg, A. M. (2020). What drives spatial variability in rainfall intensity-duration thresholds for post-wildfire debris flows? insights from the 2018 buzzard fire, nm, usa. *Landslides*, *17*(10), 2385–2399.

McKay, M. D., Beckman, R. J., & Conover, W. J. (1979). A comparison of three methods for selecting values of input variables in the analysis of output from a computer code. *Technometrics*, *21*(2), 239–245.

Moody, J. A., Ebel, B. A., Nyman, P., Martin, D. A., Stoof, C., & McKinley, R. (2015). Relations between soil hydraulic properties and burn severity. *International Journal of Wildland Fire*, *25*(3), 279–293.

Moody, J. A., Shakesby, R. A., Robichaud, P. R., Cannon, S. H., & Martin, D. A. (2013). Current research issues related to post-wildfire runoff and erosion processes. *Earth-Science Reviews*, *122*, 10–37.

Morell, K., Alessio, P., Dunne, T., & Keller, E. (2021). Sediment recruitment and redistribution in mountain channel networks by post-wildfire debris flows. *Geophysical Research Letters*, *48*(24), e2021GL095549.

Nyman, P., Sheridan, G. J., Smith, H. G., & Lane, P. N. (2011). Evidence of debris flow occurrence after wildfire in upland catchments of south-east australia. *Geomorphology*, *125*(3), 383–401.

Oakley, N. S., Cannon, F., Munroe, R., Lancaster, J. T., Gomberg, D., & Ralph, F. M. (2018). Brief communication: Meteorological and climatological conditions associated with the 9 january 2018 post-fire debris flows in montecito and carpinteria, california, usa. *Natural Hazards and Earth System Sciences*, *18*(11), 3037–3043.

Oakley, N. S., Liu, T., McGuire, L. A., Simpson, M., Hatchett, B. J., Tardy, A., ... Steinhoff, D. (2023). Toward probabilistic post-fire debris-flow hazard decision support. *Bulletin of the American Meteorological Society*.

Pak, J. H., & Lee, J.-J. (2008). A statistical sediment yield prediction model incorporating the effect of fires and subsequent storm events 1. *JAWRA Journal of the American Water Resources Association*, *44*(3), 689–699.

Patra, A. K., Bauer, A. C., Nichita, C., Pitman, E. B., Sheridan, M. F., Bursik, M., ... Renschler, C. (2005). Parallel adaptive numerical simulation of dry avalanches over natural terrain. *Journal of Volcanology and Geothermal Research*, *139*, 1–21. (doi:10.1016/j.jvolgeores.2004.06.014; available online Oct, 2004)

Perkins, J. P., Diaz, C., Corbett, S. C., Cerovski-Darriau, C., Stock, J. D., Prancevic, J. P., ... Jasperse, J. (2022). Multi-stage soil-hydraulic recovery and limited ravel accumulations following the 2017 nuns and tubbs wildfires in northern california. *Journal of Geophysical Research: Earth Surface*, *127*(6), e2022JF006591.

Rasmussen, C. E., & Williams, C. K. I. (2006). *Gaussian processes for machine learning*. Boston, MA: The MIT Press. Retrieved from `http://www.gaussianprocess.org/gpml/chapters`

Rengers, F. K., McGuire, L. A., Kean, J. W., Staley, D. M., & Hobley, D. (2016). Model simulations of flood and debris flow timing in steep catchments after wildfire. *Water Resources Research*, *52*(8), 6041–6061.

Robichaud, P. R., Wagenbrenner, J. W., Pierson, F. B., Spaeth, K. E., Ashmun, L. E., & Moffet, C. A. (2016). Infiltration and interrill erosion rates after a wildfire in western montana, usa. *Catena*, *142*, 77–88.

Roering, J. J., & Gerber, M. (2005). Fire and the evolution of steep, soil-mantled landscapes. *Geology*, *33*(5), 349–352.

Rutarindwa, R., Spiller, E. T., Bevilacqua, A., Bursik, M. I., & Patra, A. K. (2019). Dynamic probabilistic hazard mapping in the Long Valley Volcanic Region, CA: Integrating vent opening maps and statistical surrogates of physical models of pyroclastic density currents. *Journal of Geophysical Research: Solid Earth*, *124*(9), 9600–9621. doi: 10.1029/2019JB017352

Sacks, J., Schiller, S. B., & Welch, W. J. (1989). Designs for computer experiments. *Technometrics*, *31*(1), 41–47. doi: 10.1080/00401706.1989.10488474

Sacks, J., Welch, W. J., Mitchell, T. J., & Wynn, H. P. (1989). Design and analysis of computer experiments. *Statistical Science*, *4*(4), 409–423. doi: 10.1214/ss/1177012413

Santi, P. M., dewolfe, V. G., Higgins, J. D., Cannon, S. H., & Gartner, J. E. (2008). Sources of debris flow material in burned areas. *Geomorphology*, *96*(3-4), 310–321.

Santner, T. J., Williams, B. J., & Notz, W. I. (2003). *The design and analysis of computer experiments*. New York, NY: Springer-Verlag.

Shakesby, R. A., & Doerr, S. H. (2006). Wildfire as a hydrological and geomorphological agent. *Earth-Science Reviews*, *74*(3-4), 269–307.

Sheridan, G. J., Lane, P. N., & Noske, P. J. (2007). Quantification of hillslope runoff and erosion processes before and after wildfire in a wet eucalyptus forest. *Journal of Hydrology*, *343*(1-2), 12–28.

Simakov, N. A., Jones-Ivey, R. L., Akhavan-Safaei, A., Aghakhani, H., Jones, M. D., & Patra, A. K. (2019). Modernizing titan2d, a parallel amr geophysical flow code to support multiple rheologies and extendability. In *International conference on high performance computing* (pp. 101–112).

Spiller, E. T., Bayarri, M. J., Berger, J. O., Calder, E. S., Patra, A. K., Pitman, E. B., & Wolpert, R. L. (2014). Automating emulator construction for geophysical hazard maps. *SIAM/ASA Journal of Uncertainty Quantification*, *2*(1), 126–152. doi: 10.1137/120899285

Spiller, E. T., Wolpert, R. L., Ogburn, S. E., Calder, E. S., Berger, J. O., Patra, A. K., & Pitman, E. B. (2020). Volcanic hazard assessment for an eruption hiatus, or post-eruption unrest context: Modeling continued dome collapse

hazards for Soufrière Hills Volcano. *Frontiers in Earth Science: Geohazards and Georisks*, *8*(535567), 396. doi: 10.3389/feart.2020.535567

Spiller, E. T., Wolpert, R. L., Tierz, P., & Asher, T. G. (2023). The zero problem: Gaussian process emulators for range-constrained computer models. *SIAM/ASA Journal on Uncertainty Quantification*, *11*(2), 540–566. doi: 10.1137/21M1467420

Staley, D. M., Negri, J. A., Kean, J. W., Laber, J. L., Tillery, A. C., & Youberg, A. M. (2017). Prediction of spatially explicit rainfall intensity–duration thresholds for post-fire debris-flow generation in the western united states. *Geomorphology*, *278*, 149–162.

Staley, D. M., Wasklewicz, T. A., & Kean, J. W. (2014). Characterizing the primary material sources and dominant erosional processes for post-fire debris-flow initiation in a headwater basin using multi-temporal terrestrial laser scanning data. *Geomorphology*, *214*, 324–338.

Stefanescu, E. R., Bursik, M., Cordoba, G., Dalbey, K., Jones, M. D., Patra, A. K., ... Sheridan, M. F. (2012). Digital elevation model uncertainty and hazard analysis using a geophysical flow model. *Proceedings of the Royal Society A: Mathematical, Physical and Engineering Sciences*, *468*(2142), 1543–1563.

Stefanescu, E. R., Bursik, M., & Patra, A. K. (2012). Effect of digital elevation model on mohr-coulomb geophysical flow model output. *Natural hazards*, *62*(2), 635–656.

Stein, M. L. (1999). *Interpolation of spatial data*.

Stoof, C. R., Ferreira, A. J., Mol, W., Van den Berg, J., De Kort, A., Drooger, S., ... Ritsema, C. J. (2015). Soil surface changes increase runoff and erosion risk after a low–moderate severity fire. *Geoderma*, *239*, 58–67.

Stoof, C. R., Vervoort, R., Iwema, J., Van Den Elsen, E., Ferreira, A., & Ritsema, C. (2012). Hydrological response of a small catchment burned by experimental fire. *Hydrology and Earth System Sciences*, *16*(2), 267–285.

Tang, H., McGuire, L. A., Kean, J. W., & Smith, J. B. (2020). The impact of sediment supply on the initiation and magnitude of runoff-generated debris flows. *Geophysical Research Letters*, *47*(14), e2020GL087643.

Tang, H., McGuire, L. A., Rengers, F. K., Kean, J. W., Staley, D. M., & Smith, J. B. (2019). Evolution of debris-flow initiation mechanisms and sediment

sources during a sequence of postwildfire rainstorms. *Journal of Geophysical Research: Earth Surface*, *124*(6), 1572–1595.

Thomas, M. A., Rengers, F. K., Kean, J. W., McGuire, L. A., Staley, D. M., Barnhart, K. R., & Ebel, B. A. (2021). Postwildfire soil-hydraulic recovery and the persistence of debris flow hazards. *Journal of Geophysical Research: Earth Surface*, *126*(6), e2021JF006091.

Wagenbrenner, J., Robichaud, P., & Elliot, W. (2010). Rill erosion in natural and disturbed forests: 2. modeling approaches. *Water Resources Research*, *46*(10).

Welch, W. J., Buck, R. J., Sacks, J., Wynn, H. P., Mitchell, T. J., & Morris, M. D. (1992). Screening, predicting, and computer experiments. *Technometrics*, *34*(1), 15–25. Retrieved from `http://www.jstor.org/stable/1269548` doi: 10.2307/1269548

Zhao, H., Amann, F., & Kowalski, J. (2021). Emulator-based global sensitivity analysis for flow-like landslide run-out models. *Landslides*, *18*(10), 3299–3314.

Zhao, H., & Kowalski, J. (2022). Bayesian active learning for parameter calibration of landslide run-out models. *Landslides*, 1–13.